

# We are IntechOpen, the world's leading publisher of Open Access books Built by scientists, for scientists

6,900

Open access books available

186,000

International authors and editors

200M

Downloads

Our authors are among the

154

Countries delivered to

TOP 1%

most cited scientists

12.2%

Contributors from top 500 universities



WEB OF SCIENCE™

Selection of our books indexed in the Book Citation Index  
in Web of Science™ Core Collection (BKCI)

Interested in publishing with us?  
Contact [book.department@intechopen.com](mailto:book.department@intechopen.com)

Numbers displayed above are based on latest data collected.  
For more information visit [www.intechopen.com](http://www.intechopen.com)



# Plasmonic Nanoantenna Array Design

*Tao Dong, Yue Xu and Jingwen He*

## Abstract

Recently, wireless optical communication system is developing toward the chip level. Optical nanoantenna array in optical communication system is the key component for radiating and receiving light. In this chapter, we propose a sub-wavelength plasmonic nanoantenna with high gain operating at the standard optical communication wavelength of 1550 nm. The designed plasmonic antenna has a good matching with the silicon waveguide in a wide band, and light is fed from the bottom of the nanoantenna via the silicon waveguide. Furthermore, we design two kinds of antenna arrays with the proposed plasmonic nanoantenna, including one- and two-dimensional arrays ( $1 \times 8$  and  $8 \times 8$ ). The radiation characteristics of the antenna arrays are investigated and both arrays have high gains and wide beam steering range without grating lobes.

**Keywords:** plasmonic nanoantenna, localized surface plasmon, integrated optical antenna arrays, integrated photonic devices, radiation characteristics

## 1. Introduction

In recent years, silicon-based integrated photonic devices have been developing rapidly. In particular, integrated optical antenna arrays have broad application prospect in many fields, such as optical communication, light detection and ranging (LiDAR), vehicle autonomous driving, security monitoring, and display advertising [1–5]. Nanoantenna is a key part of the optical antenna array for converting guided light and free space light with specific directivity. Based on the light interference principle, beam steering is realized by controlling the phase of the light radiated by each nanoantenna in the optical antenna array. In order to realize optical phase control, the concept of optical phased array (OPA) is proposed [6–8]. In the field of silicon-based photonics, OPA is a highly integrated on-chip system, which consists of light division network, phase shifters, and optical antenna array [9–11]. In optical communication, OPA is required to have high gain, narrow beam, and wide steering range. However, at present, monolithic integrated OPAs suffer from low gain, small beam steering range, and wide beam width, which are mainly due to the low radiation efficiency of the nanoantenna, the large element spacing (the spacing between adjacent antenna in the antenna array), and the limited scale of the optical antenna array [12, 13].

The most commonly used silicon-based nanoantenna in the integrated optical antenna array is dielectric grating antenna. Generally, dielectric grating antenna refers to the periodic micro/nanostructure etched on dielectric substrate.

The existing dielectric grating antenna suffers from large footprint and bidirectional radiation, which result in large element spacing and waste of radiation energy of the optical nanoantenna array [14–18]. In a uniform antenna array, the element spacing larger than the operating wavelength will lead to the appearance of grating lobes in the radiation pattern of the antenna array, which will limit the steering range of the optical nanoantenna array.

In order to obtain a miniaturized optical antenna with high radiation efficiency, plasmonic nanoantenna is proposed [19–22]. Plasmonic nanoantenna is composed of metal and dielectric. When electromagnetic wave impinges on the interface of metal and dielectric, it will couple and oscillate with the surface electrons of the metal, and surface plasmon polarization (SPP) is generated. When SPP is unable to transmit along the interface and is confined, the SPP is called localized surface plasmon (LSP). LSP can confine the electromagnetic wave into a space far less than a wavelength. Based on the LSP resonance effect, electromagnetic wave will be enhanced and radiated into free space by plasmonic antenna. Taking advantage of this character, plasmonic nanoantennas can realize a tiny size [22]. However, the traditional plasmonic nanoantennas [20, 22] are fed by plasmonic waveguides, in which the impedance matching band is narrow and high loss is introduced. In addition, the traditional plasmonic nanoantenna does not radiate light along the direction perpendicular to the plane where the antenna is located, which also limits the light steering range of the optical nanoantenna array [1, 2, 20, 22].

In this chapter, we propose a plasmonic nanoantenna with sub-wavelength footprint and high gain operating at the standard optical communication wavelength of 1550 nm, i.e., 193.5 THz [23]. The proposed plasmonic nanoantenna consists of a silver block and a silicon block, and its footprint is much smaller than that of dielectric grating antenna. Unlike recent studies on the plasmonic nanoantennas, an impedance matching between the proposed plasmonic nanoantenna and a silicon waveguide is achieved in a wide band. Light is fed from the bottom of the plasmonic nanoantennas by the silicon waveguide and is radiated vertically upward without bidirectional radiation. This kind of bottom fed plasmonic nanoantenna is suitable for the expansion of the nanoantenna array. Based on the proposed plasmonic nanoantenna, two plasmonic nanoantenna arrays including  $1 \times 8$  and  $8 \times 8$  arrays are designed. The radiation characteristics of the plasmonic nanoantenna arrays are simulated and discussed in detail.

## 2. Plasmonic nanoantenna

### 2.1 Radiation characteristics of the designed plasmonic nanoantenna

**Figure 1** illustrates the schematic diagram of the proposed plasmonic nanoantenna. The plasmonic nanoantenna is composed of silicon (Si) block, silver (Ag) block, and a silicon waveguide with a silicon dioxide ( $\text{SiO}_2$ ) coating. As shown in **Figure 1**, a silicon waveguide through the silver block is connected with the silicon block for feeding light into the plasmonic nanoantenna. The lengths of the silicon waveguide along the  $x$ - and  $y$ -axis are 450 nm and 220 nm respectively, which are suitable for the light propagation with high efficiency. In each block, the length of the edge along the  $x$ - and  $y$ -axis is defined as width and length. The width, length, and height of the silicon block are represented by  $W_1$ ,  $L_1$ , and  $H_{\text{Si}}$ , respectively. Similarly, the parameters  $W_2$ ,  $L_2$ , and  $H_{\text{Ag}}$  represent the width, length, and height of the silver block, respectively. The geometric parameters of the nanoantenna are as follows:  $W_1 = 625$  nm,  $L_1 = 850$  nm,  $H_{\text{Si}} = 300$  nm,  $W_2 = 1100$  nm,  $L_2 = 1100$  nm, and  $H_{\text{Ag}} = 200$  nm.

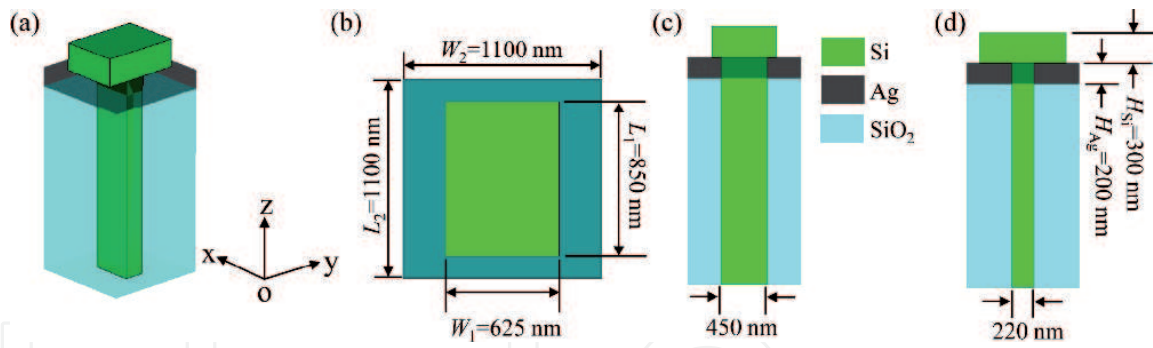


**Figure 1.** The plasmonic nanoantenna in the (a) perspective, (b) overhead, (c) front, and (d) side views.

Some electromagnetic simulations for investigating the radiation characteristics of the plasmonic nanoantenna are performed with the commercial software of CST-Microwave Studio. For simulation, a beam of light with TE polarization ( $x$ -polarization) is fed into the plasmonic nanoantenna via the silicon waveguide. At the frequency of 193.5 THz, the relative dielectric constants of the materials of silicon and silicon dioxide are 12.11 and 2.1, respectively. The relative dielectric constant of silver is  $-129 + j3.28$  at 193.5 THz [24]. Due to the small imaginary part and the large real part, silver has a very low ohmic loss that makes it an ideal metal to generate LSP.

**Figure 2** shows the simulated optical field distributions in the cross-sections of the designed plasmonic nanoantenna at the frequency of 193.5 THz. **Figure 2(a)** and **(b)** illustrates the optical fields in the  $x$ - $o$ - $y$  cross section and  $x$ - $o$ - $z$

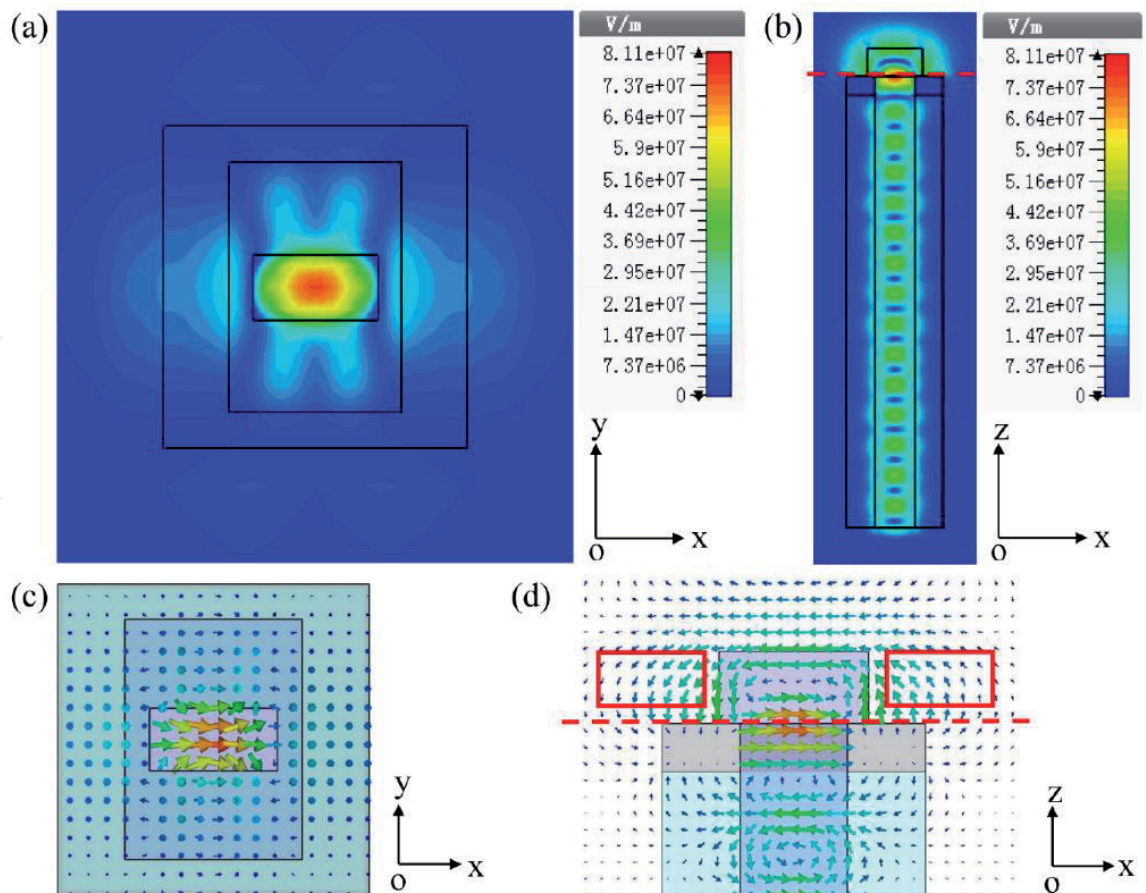


**Figure 2.** Simulated optical field in the (a)  $x$ - $o$ - $y$  cross-section and (b)  $x$ - $o$ - $z$  cross-section of the designed plasmonic nanoantenna at 193.5 THz. Optical field vector distribution maps in the (c)  $x$ - $o$ - $y$  and (d)  $x$ - $o$ - $z$  cross-sections of the nanoantenna at 193.5 THz.

cross-section, respectively. **Figure 2(a)** represents the interface of the silicon and silver blocks marked by a red dashed line in **Figure 2(b)**. As shown in **Figure 2(b)**, the optical field changes periodically in the silicon waveguide and an optical enhancement happens at the interface of the silicon and silver blocks. Such a field distribution indicates that the light propagates along the silicon waveguide until it reaches the junction of the silver and silicon blocks. Due to the introduction of metallic material silver, SPPs are generated on the surface of the silver block and localized surface plasma resonance (LSPR) occurs at 193.5 THz. The LSPR results in the enhancement of the optical field and the radiation of the nanoantenna.

The optical vector distribution maps in the  $x$ - $o$ - $y$  and  $x$ - $o$ - $z$  cross-sections are displayed in **Figure 2(c)** and **(d)**, respectively. **Figure 2(c)** represents the interface of the silicon and silver blocks marked by a red dashed line in **Figure 2(b)**. As shown in the areas marked by two red boxes in **Figure 2(d)**, the optical vector fields in the regions on both sides of the silicon block point up and down, respectively. The optical vector fields in the opposite direction indicate that the phase difference of the optical fields on both sides of the silicon block is  $180^\circ$ . Therefore, the optical fields are superposed above the plasmonic nanoantenna.

Radiation characteristics of the plasmonic nanoantenna in **Figure 1** including far-field radiation pattern, gain, and return loss are analyzed by using electromagnetic simulation. **Figure 3** displays the far-field radiation pattern of the designed plasmonic nanoantenna at 193.5 THz. The parameters  $\theta$  and  $\varphi$  represent the elevation and azimuth angles in free space, respectively. It is clearly seen that light is radiated vertically. The plasmonic nanoantenna has a smooth main lobe without bidirectional radiation. In order to observe clearly, the far-field radiation patterns in two orthogonal planes of  $\varphi = 0^\circ$  ( $x$ - $o$ - $z$ ) and  $\varphi = 90^\circ$  ( $y$ - $o$ - $z$ ) at 193.5 THz are extracted and displayed in **Figure 4(a)**. The black and blue curves indicate the far-field radiation pattern in the planes of  $\varphi = 0^\circ$  and  $\varphi = 90^\circ$ , respectively. The two curves coincide at  $\theta = 0^\circ$  indicating a vertical radiation with a gain of 8.45 dB. On the two planes of  $\varphi = 0^\circ$  and  $\varphi = 90^\circ$ , the half-power beam widths (HPBW) of the main lobe are  $51.3^\circ$  and  $43.7^\circ$ , respectively. The return loss of the designed plasmonic nanoantenna is shown in **Figure 4(b)**. It can be found that the return loss is less than  $-10$  dB in the frequency range from 176.7 to 248.5 THz, which means that the designed plasmonic nanoantenna has a good matching with the silicon waveguide within a bandwidth of 71.8 THz.

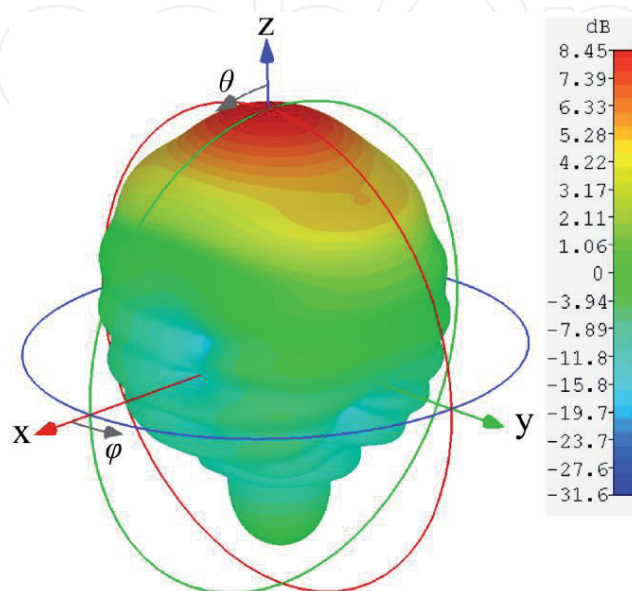


**Figure 3.** Far-field radiation pattern of the plasmonic nanoantenna at 193.5 THz.

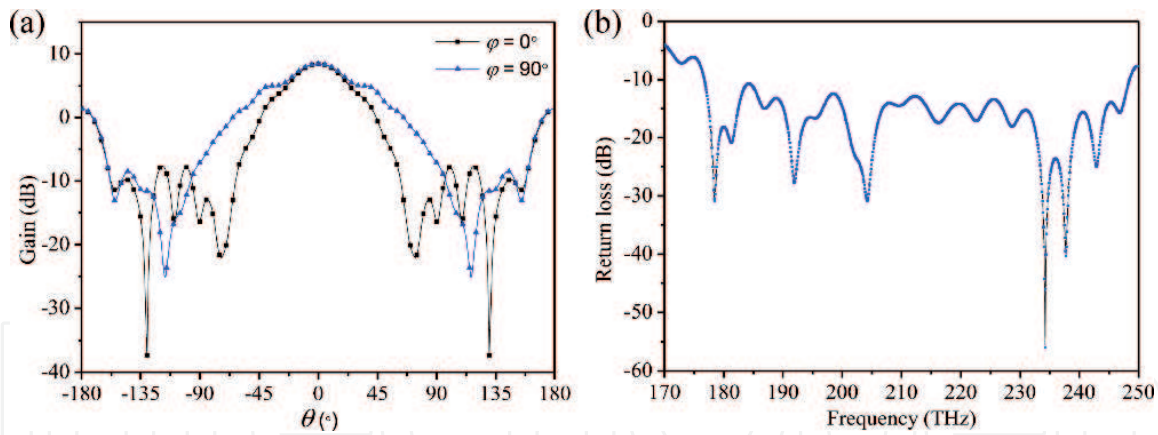


**Figure 4.** (a) Far field radiation patterns in the planes of  $\varphi = 0^\circ$  and  $\varphi = 90^\circ$  and (b) return loss of the designed plasmonic nanoantenna at 193.5 THz.

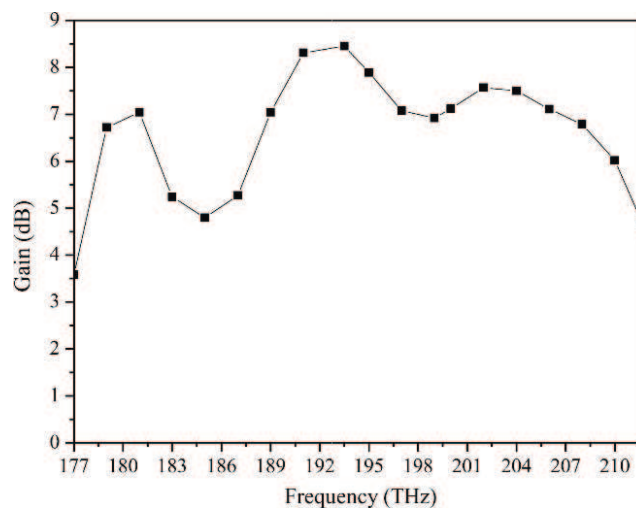


**Figure 5.** Gain of the designed plasmonic nanoantenna at the frequency range of 177–212 THz.

Gain is an important radiation characteristic of the optical antennas, which represents the ability of an antenna to radiate optical power in a given direction. **Figure 5** shows the calculated gain of the designed plasmonic nanoantenna. It is clearly seen that at the center frequency of 193.5 THz, the gain of the antenna reaches its maximum value of 8.45 dB.

## 2.2 Parameter analysis of the plasmonic nanoantenna

In order to understand the impacts of the geometric parameters of the silicon and silver blocks on the radiation characteristics of the plasmonic nanoantenna, a series of electromagnetic simulations are performed and the simulation results are analyzed in detail. We choose the plasmonic nanoantenna mentioned above ( $W_1 = 625$  nm,  $L_1 = 850$  nm,  $H_{Si} = 300$  nm,  $W_2 = 1100$  nm,  $L_2 = 1100$  nm, and  $H_{Ag} = 200$  nm) as the simulation model.

Firstly, the influences of the width ( $W_1$ ) and length ( $L_1$ ) of the silicon block in the plasmonic nanoantenna on the gain are analyzed, and the results are given in **Figure 6**. **Figure 6(a)** shows the variation of the gain with the width of the silicon block ( $W_1$ ) increasing from 545 to 705 nm. It can be found that the gain increases first and decreases with the increase of  $W_1$ , and the gain reaches the maximum value of 8.45 dB when  $W_1 = 625$  nm. It also proves that the width of 625 nm satisfies the condition of electromagnetic resonance. Similarly, the variation of the gain with the

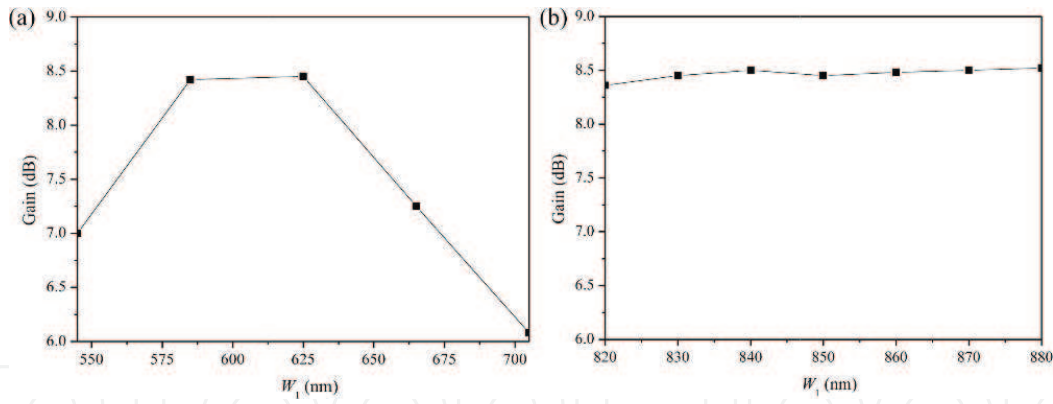


**Figure 6.** The simulated gain of the plasmonic nanoantenna varies with (a) the width  $W_1$  and (b) the length  $L_1$  of the silicon block at the frequency of 193.5 THz, respectively.

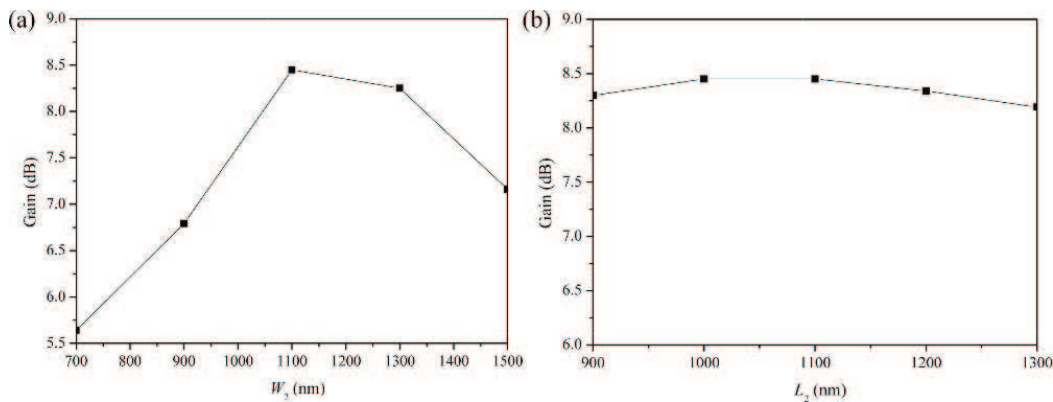


**Figure 7.** The simulated gain of the plasmonic nanoantenna varies with (a) the width  $W_2$  and (b) the length  $L_2$  of the silver block at the frequency of 193.5 THz, respectively.

length of the silicon block ( $L_1$ ) increasing from 820 to 880 nm is studied, as shown in **Figure 6(b)**. It can be seen that the length of the silicon block ( $L_1$ ) has little effect on the gain. Since the polarization state of the incident light is TE mode (the polarization direction along to the  $x$ -axis), the electromagnetic resonance is determined by the geometric dimension along the  $x$ -axis. Therefore, the influence of the width of the silicon block on the gain is more obvious than that of the length of the silicon block.

Secondly, the influences of the width ( $W_2$ ) and length ( $L_2$ ) of the silver block in the plasmonic nanoantenna structure on the gain are analyzed, and the results are given in **Figure 7**. **Figure 7(a)** displays the variation of the gain with the width of the silver block ( $W_2$ ) increasing from 700 to 1550 nm. The variation of the gain with the length of the silver block ( $L_2$ ) increasing from 900 to 1300 nm is shown in **Figure 7(b)**. It is clearly seen that when  $W_2$  is increased, the gain will increase first and then decrease. The increase of the width of the silver block means the increase of the antenna aperture, which will result in the increase of the gain. However, in the proposed nanoantenna, the gain will decrease when  $W_2$  and  $L_2$  are larger than 1100 nm because of high absorption loss of metal in optical wavelength. The length of the silver block has little effect on the gain, which depends on the polarization state of the incident light.

Finally, the influences of the heights of the silicon block ( $H_{Si}$ ) and silver block ( $H_{Ag}$ ) in the plasmonic nanoantenna structure on the gain are also analyzed, as shown in **Figure 8(a)** and **(b)**, respectively. When  $H_{Si}$  and  $H_{Ag}$  are increased, the gain of the antenna increases first and then decreases. Compared with the silver block, the height of the silicon block has a greater influence on the gain. The gain reaches the maximum when  $H_{Si} = 300$  nm and  $H_{Ag} = 200$  nm, respectively.

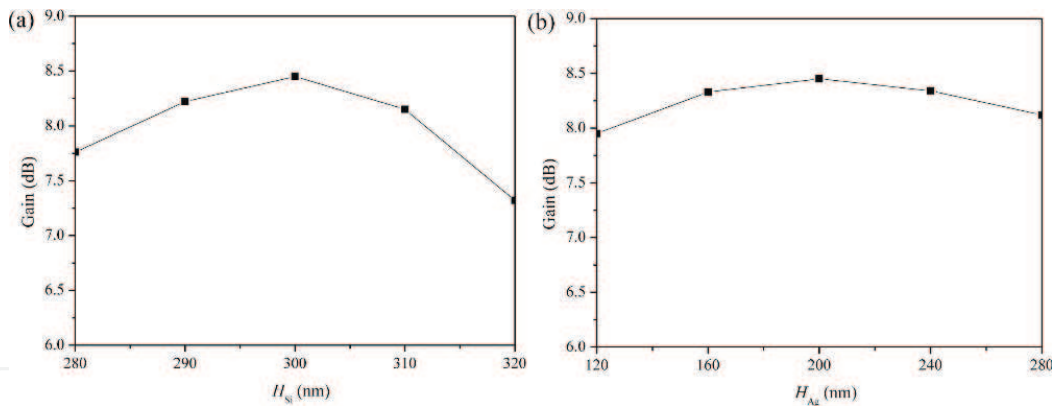


**Figure 8.** The simulated gain of the plasmonic nanoantenna varies with the heights of the (a) silicon and (b) silver block at the frequency of 193.5 THz.

The simulation results show that the geometric parameters of the silver and silicon blocks will affect the radiation characteristics of the antenna. For TE polarized incident wave, the widths of the silicon and silver blocks have significant effect on the gain, and the lengths of the silicon and silver blocks have little effect on the gain. It is necessary to optimize these parameters to obtain a plasmonic nanoantenna with high gain.

### 3. Plasmonic nanoantenna arrays

In practical applications, the antenna array is used to realize beam steering on the basis of the optical field superposition principle. The beam deflection is realized by changing the phase of the light radiated by each antenna in the array. Usually, radiation characteristics of the antenna array, including steering angle, beam width, gain, return loss, and mutual coupling between each antenna [25] should be considered. Utilizing the proposed plasmonic nanoantenna, one-dimensional (1-D) and two-dimensional (2-D) arrays are designed, and their radiation characteristics are investigated in detail.

#### 3.1 $1 \times 8$ plasmonic nanoantenna array

In the research of 1-D array, a  $1 \times 8$  array is designed using the proposed plasmonic nanoantenna, as shown in **Figure 9**. In the  $1 \times 8$  array, the nanoantennas are arranged in a row along the  $x$ -axis with element spacing of  $d$ . In the simulation, optical signals are fed from the waveguide port of each antenna, i.e., Port1 to Port8, respectively. For the array with uniform element spacing, the element spacing larger than one wavelength will lead to the appearance of the grating lobes in the far-field radiation pattern of the array, which will limit the beam steering range. In our design, the element spacing is set to  $0.7\lambda_0$  (i.e.,  $d = 1085$  nm), which is much smaller than the element spacing reported in Ref. [1]. Thus, the whole  $1 \times 8$  array is 8680 nm in length and 1085 nm in width.

The return loss of each waveguide port in the designed  $1 \times 8$  array is calculated and shown in **Figure 10**. The curves S11 to S88 represent the return losses of Port1 to Port8, respectively. The results in **Figure 10** show that the return losses of all ports are less than  $-22.5$  dB in the frequency region 191.5–196.2 THz. It means that the reflectivity of each port is less than 0.6%. Such low return losses also prove that there is a good impedance match between the designed plasmonic nanoantenna and the silicon waveguide in a wide bandwidth. To research the coupling effect

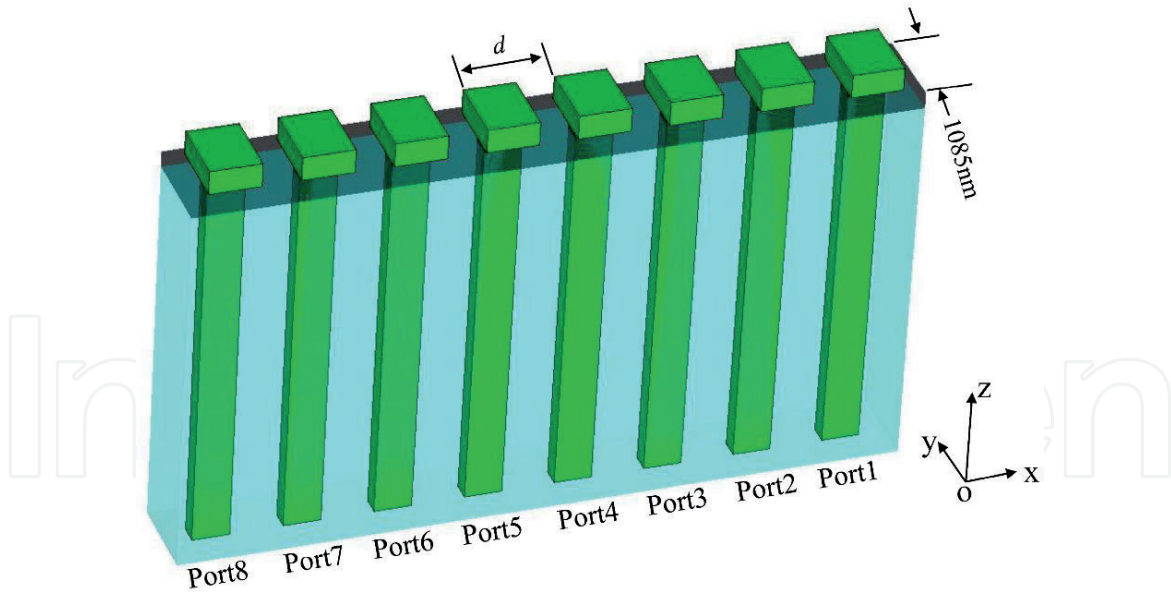


**Figure 9.**  
Structure of  $1 \times 8$  array.

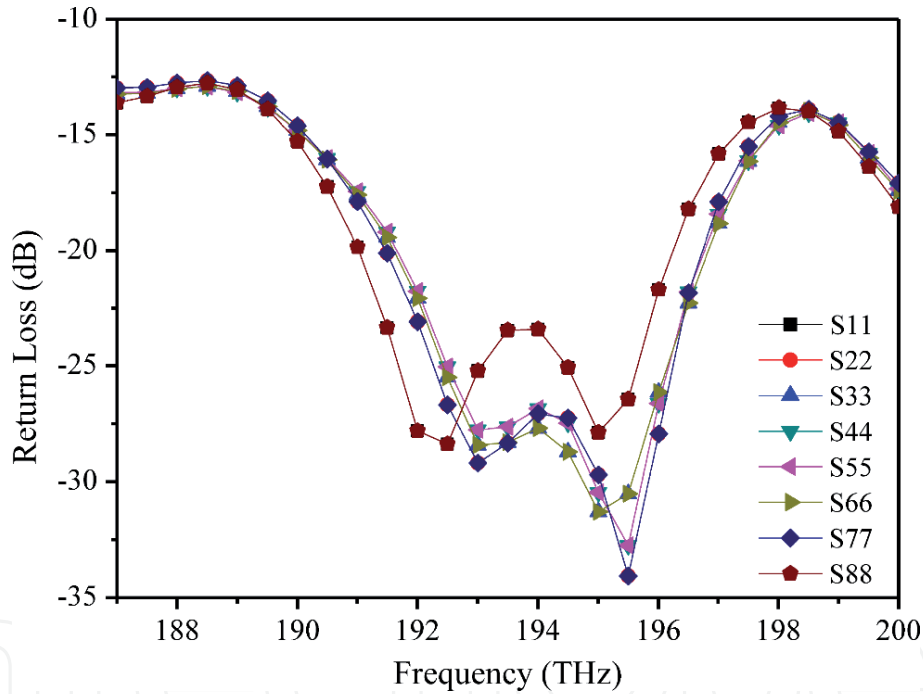


**Figure 10.**  
Return losses of the ports from Port1 to Port8 in the  $1 \times 8$  array with  $d = 0.7\lambda_0$ .

among the ports, the mutual couplings between other ports and Port1 are shown in **Figure 11**. The mutual coupling decreases as the distance between Port1 and other ports increases at 193.5 THz.

In the simulation, the radiation pattern of the  $1 \times 8$  array is studied by feeding optical signals with the equal amplitude and the same phase into each port simultaneously. **Figure 12(a)** and **(b)** display the far-field radiation patterns of the  $1 \times 8$  array in the planes of  $\varphi = 0^\circ$  and  $\varphi = 90^\circ$  at 193.5 THz, respectively. The simulation results show that the  $1 \times 8$  array radiates light vertically upward with a gain of 14.5 dB and the HPBW of the main lobe on the planes of  $\varphi = 0^\circ$  and  $\varphi = 90^\circ$  are  $9.0^\circ$  and  $96.4^\circ$ , respectively.

According to the filed superposition principle, beam steering can be realized by changing the phase of light radiated by each antenna in the antenna array. In theory,

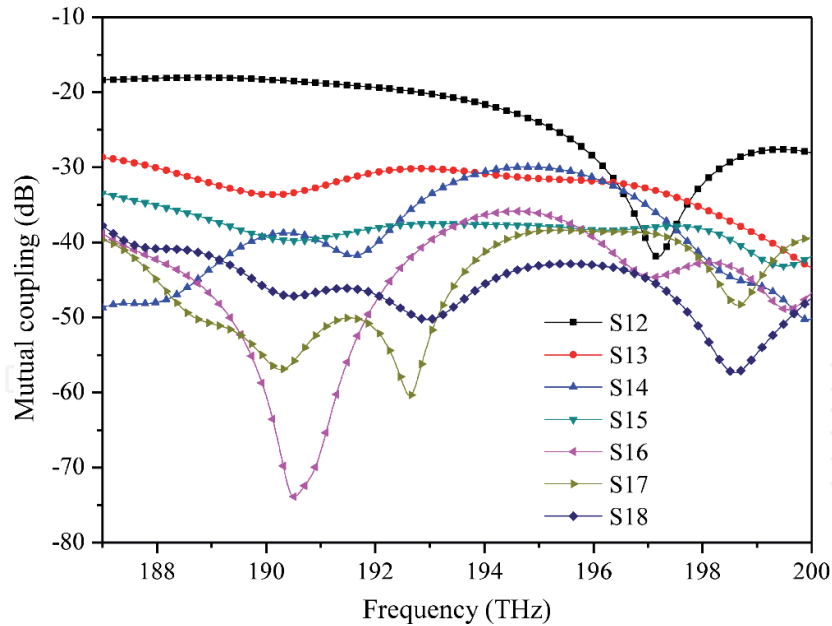


**Figure 11.**  
 The mutual coupling between other ports and port1.

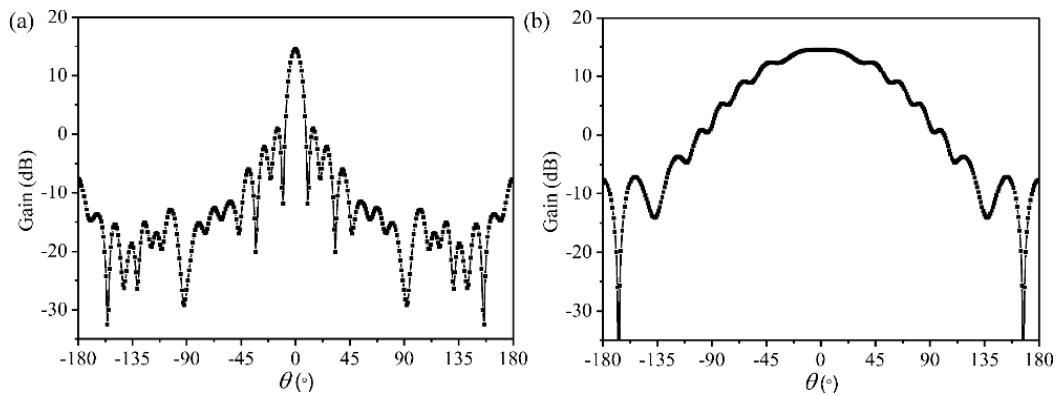


**Figure 12.**  
 Far-field radiation patterns of the  $1 \times 8$  array with  $d = 0.7\lambda_0$  in the planes of (a)  $\varphi = 0^\circ$  and (b)  $\varphi = 90^\circ$  at the frequency of 193.5 THz.

for a 1-D array along the  $x$ -axis with uniform element spacing  $d$ , the relationship between the beam steering angle  $\theta$  and the phase difference of light fed into the two adjacent antennas  $\psi_x$  follows the equation of [25]

$$kd \sin\theta = \psi_x, \quad (1)$$

where the parameter  $k$  represents wave vector in the free space.

We further study the beam steering characteristics of the  $1 \times 8$  array in **Figure 9** by using the methods of electromagnetic simulation and theoretical calculation. At 193.5 THz, the far-field radiation pattern of the  $1 \times 8$  array in the plane of  $\varphi = 0^\circ$  with various phase difference of the input light fed in two adjacent antennas  $\psi_x$  is simulated, as shown in **Figure 13**. The simulation results show that when the phase difference  $\psi_x$  increases from  $-180^\circ$  to  $+180^\circ$  with an interval of  $45^\circ$ , the beam steers from  $-44^\circ$  to  $+44^\circ$  in the  $\varphi = 0^\circ$  plane. When the light fed into each antenna has the same phase, i.e.,  $\psi_x = 0^\circ$ , the plasmonic nanoantenna array radiates light in the direction of  $\theta = 0^\circ$  with the highest gain and the narrowest beam width. As beam steering angle increases, the main lobe width of the radiation beam increases, and the gain decreases. When the phase difference is  $\pm 180.0^\circ$ , i.e.,  $\psi_x = 180^\circ$ , the peak

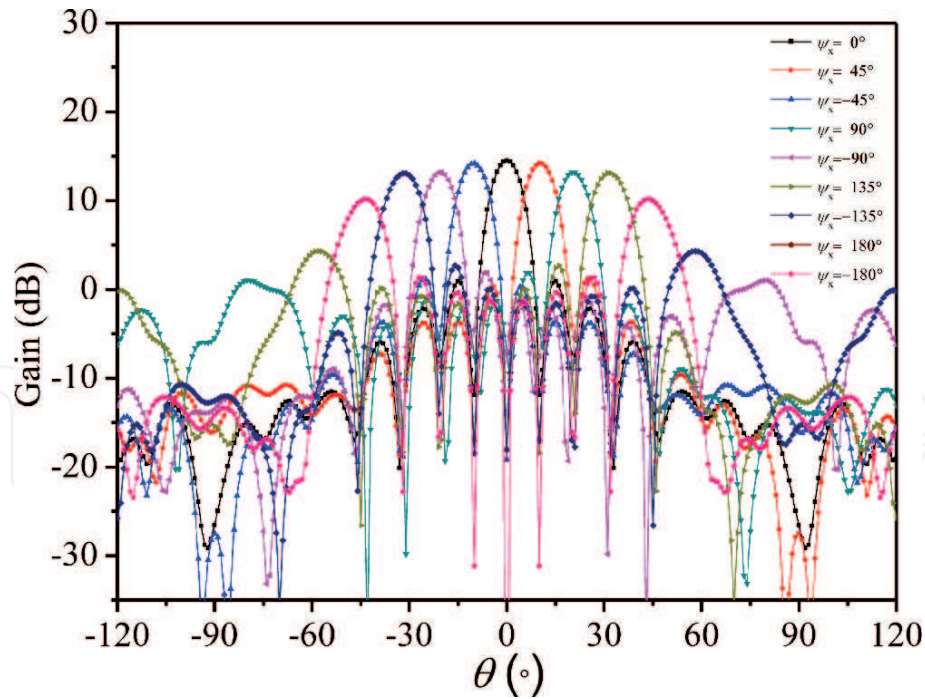


**Figure 13.** Far-field beam steering of the  $1 \times 8$  array with  $d = 0.7\lambda_0$  in the plane of  $\varphi = 0^\circ$  with various phase differences at 193.5 THz.

value of the grating lobe of the radiation light is the same as that of the main lobe, and the beam steering angle is  $\pm 44.0^\circ$ , which is almost consistent with the theoretical value of  $\pm 45.6^\circ$  calculated by Eq. (1). **Figure 14** gives the far-field radiation pattern of the  $1 \times 8$  array at 193.5 THz, when  $\psi_x = 45^\circ$ . As can be seen from **Figure 14**, the deflection angle of the main lobe is  $10.48^\circ$ . Theoretically, the beam steering angle obtained from Eq. (1) is  $10.28^\circ$ . The small deviation between the simulation results and theoretical results result from the mutual coupling between the nanoantennas in the array.

In a uniformly arranged array, element spacing is the critical factor for determining the radiation characteristics of the array. Numerical simulations of the  $1 \times 8$  array with different element spacing  $d$  are performed, and the influences of element spacing on the radiation characteristics are analyzed in depth.

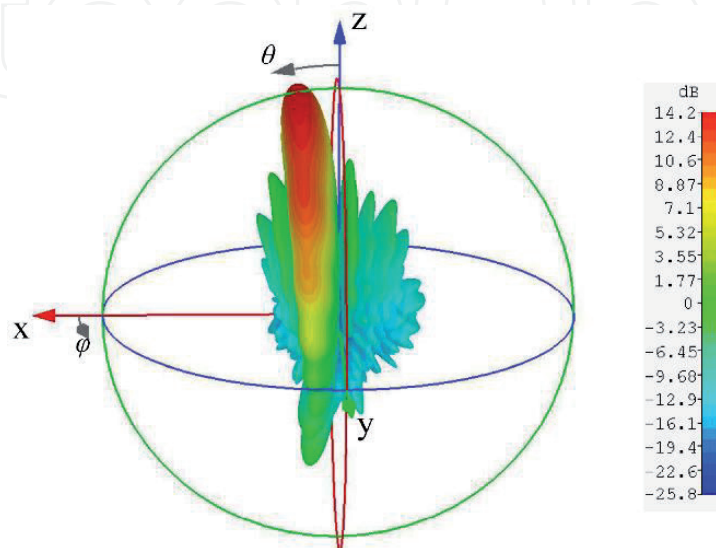


**Figure 14.** Far-field radiation pattern of the  $1 \times 8$  array with  $d = 0.7\lambda_0$  at 193.5 THz when  $\psi_x = 45^\circ$ .

The calculated S-Parameters of the  $1 \times 8$  array with different element spacing are displayed in **Figures 15** and **16**. **Figure 15(a)** and **(b)** show the return loss of Port1 ( $S_{11}$ ) and Port4 ( $S_{44}$ ) when  $d$  varies from  $0.7\lambda_0$  to  $1.1\lambda_0$ , respectively. In the frequency range of 187–200 THz, the return loss of Port1 is less than  $-12$  dB, which indicates that Port1 has good matching characteristics with different element spacing. When the element spacing is  $0.7\lambda_0$ , the return loss decreases sharply near 193.5 THz. The mutual coupling between the Port1 and the Port2 ( $S_{21}$ ) is shown in **Figure 16**. At 193.5 THz, the mutual coupling decreases with the increase of the element spacing.

The calculated far-field radiation patterns of the  $1 \times 8$  array with the phase difference  $\psi_x = 0^\circ$  in the  $\varphi = 0^\circ$  plane and  $\varphi = 90^\circ$  plane when  $d$  increases from  $0.7\lambda_0$  to  $1.1\lambda_0$  are shown in **Figure 17(a)** and **(b)**, respectively. As can be seen from **Figure 17(a)**, when the element spacing is  $1.1\lambda_0$ , the grating lobes appear at  $-62.0^\circ$  and  $62.5^\circ$ .

The far-field radiation patterns of the  $1 \times 8$  array with  $d = 0.7\lambda_0$  at three frequencies of lower side frequency 187 THz, center frequency 193.5 THz, and upper side frequency 200 THz when  $\psi_x = 0^\circ$  are shown in **Figure 18**. **Figure 18(a)** and **(b)** displays the far-field radiation patterns in the planes of  $\varphi = 0^\circ$  and  $\varphi = 90^\circ$ , respectively. The calculated results show that  $1 \times 8$  array also has almost the same gains at center and side frequencies.

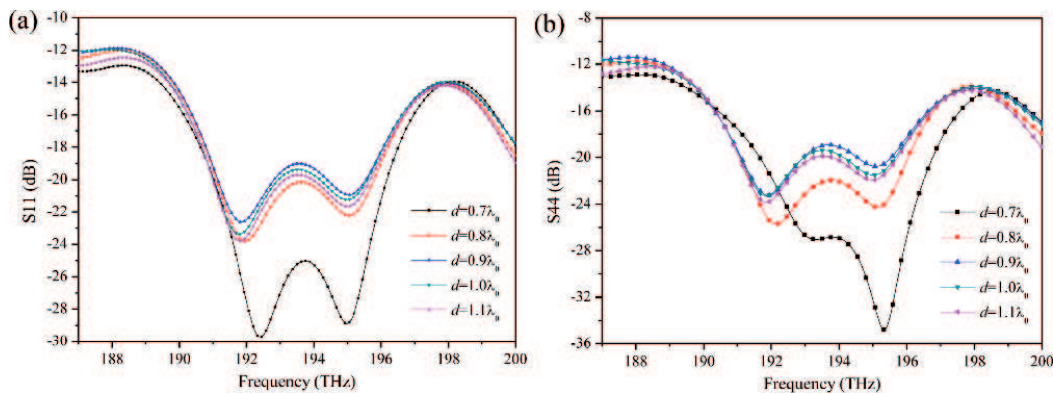


**Figure 15.**  
 Return loss of the (a) Port1 and (b) Port4.

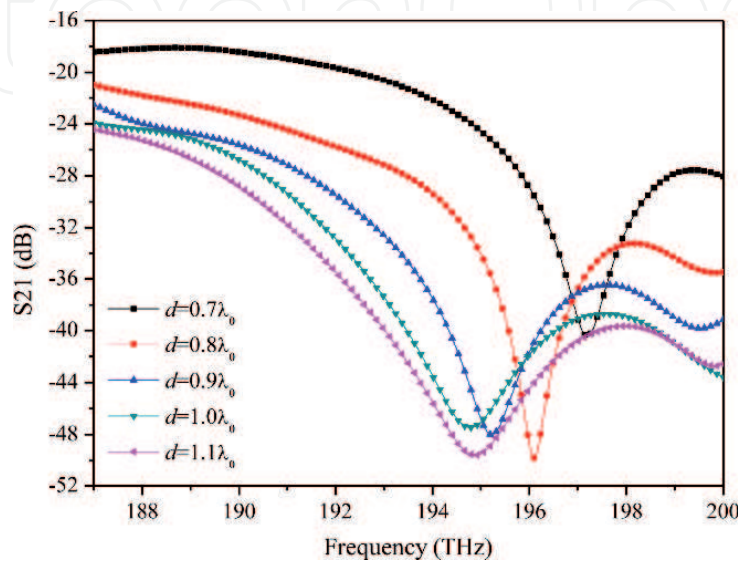


**Figure 16.**  
 Mutual coupling between the Port1 and the Port2.

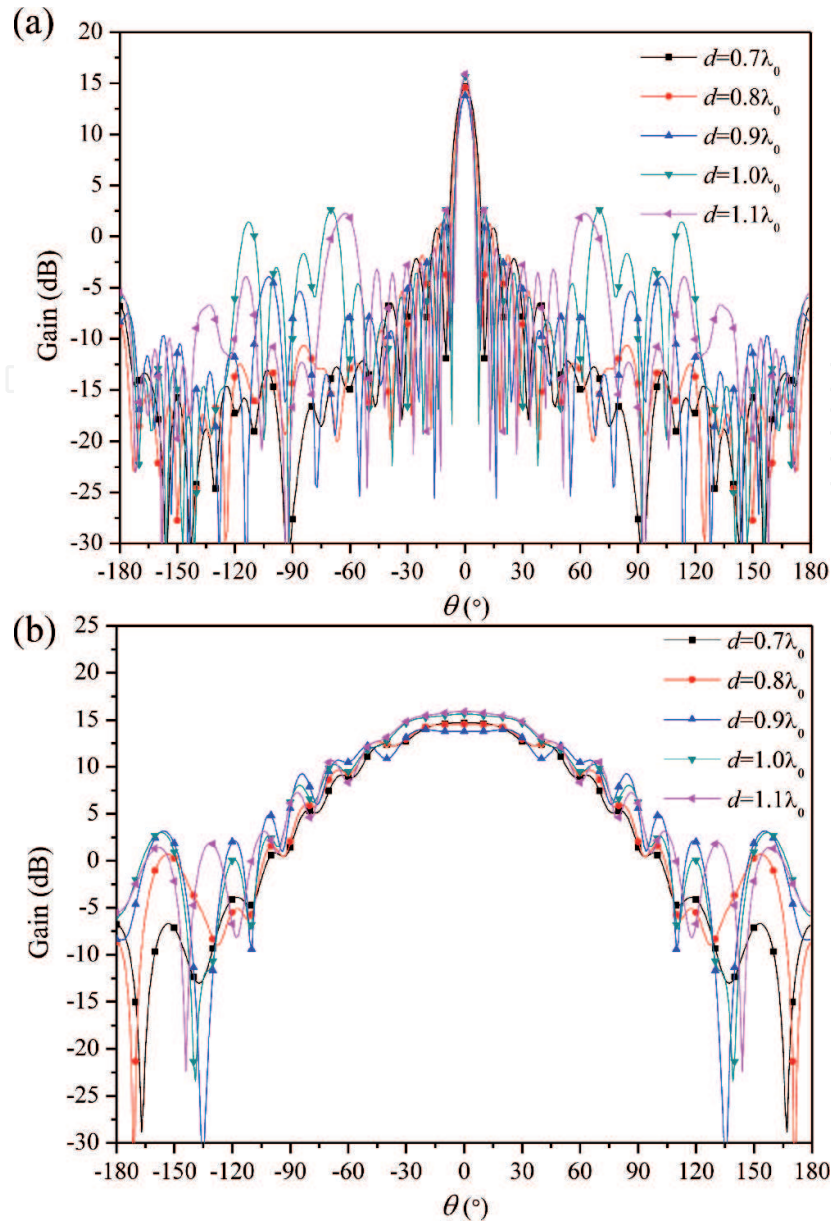


**Figure 17.**

Far-field radiation patterns of the  $1 \times 8$  array with  $\psi_x = 0^\circ$  in the planes of (a)  $\varphi = 0^\circ$  and (b)  $\varphi = 90^\circ$  when  $d$  increases from  $0.7\lambda_0$  to  $1.1\lambda_0$  at 193.5 THz.

### 3.2 $8 \times 8$ plasmonic nanoantenna array

In this section, we take the  $1 \times 8$  array mentioned above as a sub-array and extend it along the  $y$ -axis to obtain an  $8 \times 8$  array, as shown in **Figure 19**. In the  $8 \times 8$  array, the spacing between two adjacent antennas is set to  $0.7\lambda_0$  in both directions of  $x$ - and  $y$ -axis, that means the element spacing is  $d_x = d_y = 0.7\lambda_0$ . The far-field radiation pattern of a 2-D array can be calculated by using the pattern multiplication, which is given by [1]

$$E(\theta, \varphi) = S(\theta, \varphi) \times F_a(\theta, \varphi), \quad (2)$$

where  $E(\theta, \varphi)$  and  $S(\theta, \varphi)$  represent the far field radiation patterns of the 2-D array and the 1-D sub-array, respectively. The function  $F_a(\theta, \varphi)$  indicates the array factor of the 2-D array. The array factor is determined by the 1-D sub-array spacing and the number of the 1-D sub-arrays in the 2-D array along the extend direction, and the amplitude and phase of the light fed in each antenna. According to Eq. (2), the far-field radiation pattern of the  $8 \times 8$  array with constant amplitude and same

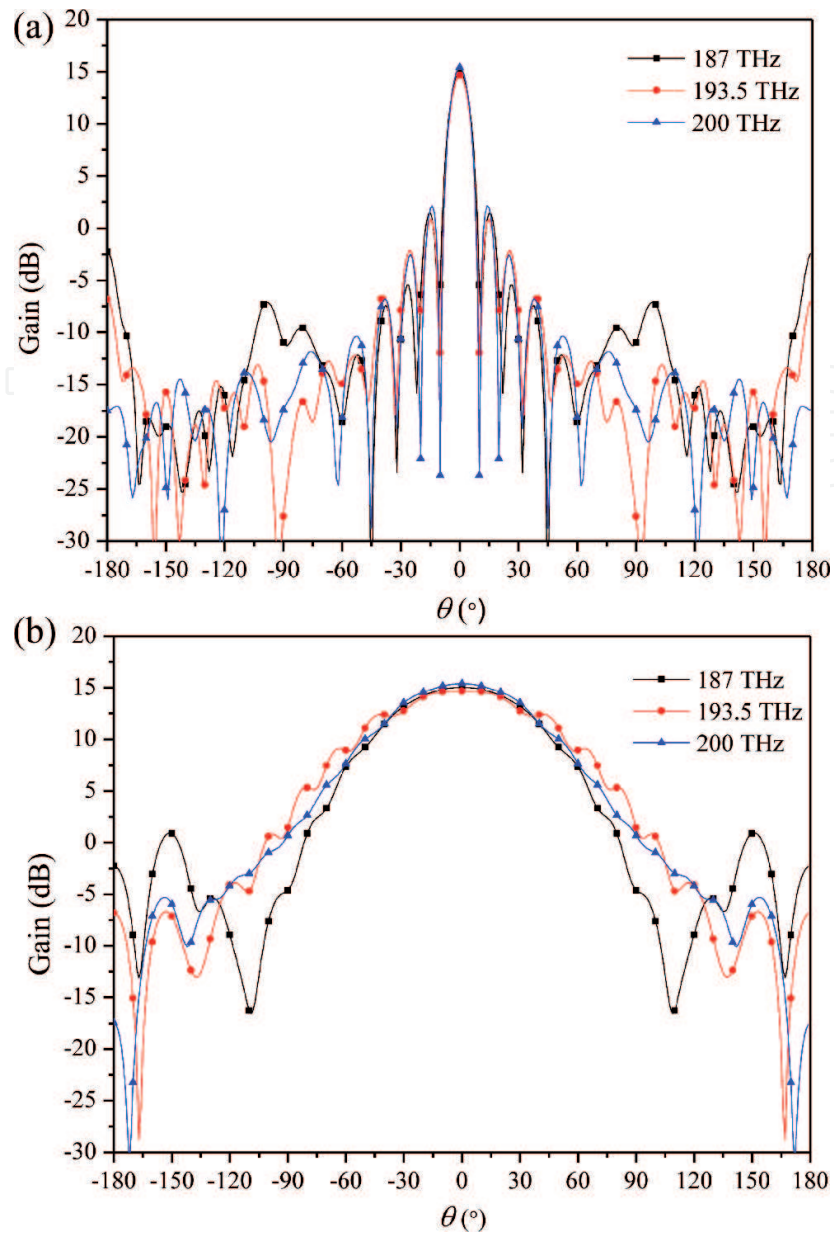


**Figure 18.** Far-field radiation patterns of the  $1 \times 8$  array with  $d = 0.7\lambda_0$  in the planes of (a)  $\varphi = 0^\circ$  and (b)  $\varphi = 90^\circ$  at three frequencies when  $\psi_x = 0^\circ$ .

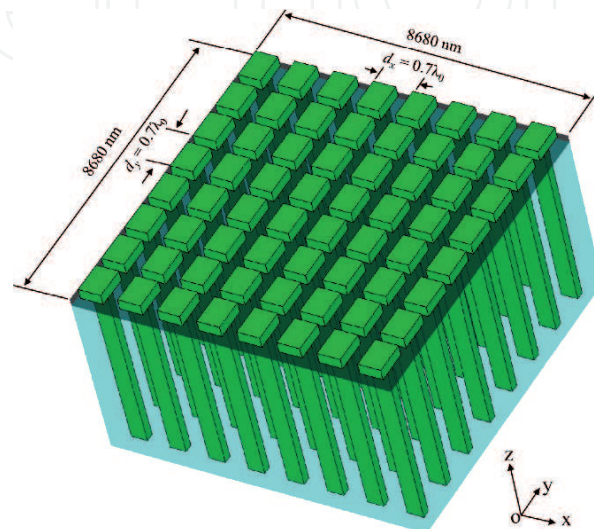


**Figure 19.** Structure of the  $8 \times 8$  array with the element spacing of  $0.7\lambda_0$  in the directions of  $x$ - and  $y$ -axis.

phase of light in each antenna at 193.5 THz is obtained. The calculated far-field radiation patterns in the planes of  $\varphi = 0^\circ$  and  $\varphi = 90^\circ$  are displayed in **Figure 20(a)** and **(b)**, respectively. It can be seen that the  $8 \times 8$  array radiates light upward with a gain of 24.2 dB and an HPBW of  $9.0^\circ \times 9.0^\circ$  at 193.5 THz.

Similar to the 1-D beam steering, 2-D beam steering of the  $8 \times 8$  array is realized by changing the phases of light in the nanoantennas along the two orthogonal directions. The parameters  $\psi_x$  and  $\psi_y$  are used to represent the phase differences between two lights fed in the adjacent nanoantennas along the  $x$ - and  $y$ -directions, respectively. When the phase difference  $\psi_x$  is changed, the beam steers in the  $\varphi = 0^\circ$  plane. **Figure 21** shows the far-field beam steering radiation patterns of the  $8 \times 8$  array in the  $\varphi = 0^\circ$  plane under various  $\psi_x$ , when  $\psi_y$  is fixed at  $0^\circ$ . It can be found that the radiation direction of the light changes in a certain range of  $-44.0^\circ$  to  $+44.0^\circ$ , as the phase difference  $\psi_x$  changes from  $-180.0^\circ$  to  $+180.0^\circ$ .

**Figure 22** shows the far-field beam steering of the  $8 \times 8$  array in the  $\varphi = 90^\circ$  plane under various  $\psi_y$ , when  $\psi_x$  is fixed at  $0^\circ$ . When the phase difference  $\psi_y$  is

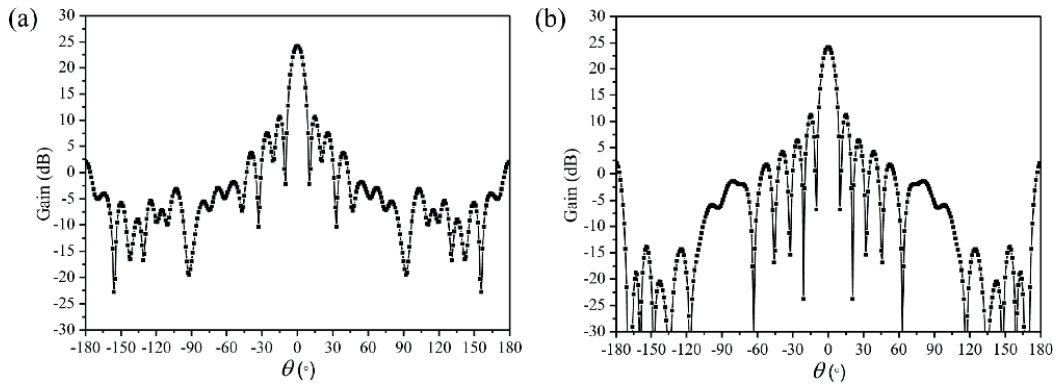


**Figure 20.**

Far-field radiation patterns of the  $8 \times 8$  array with  $d_x = d_y = 0.7\lambda_0$  in the planes of (a)  $\varphi = 0^\circ$  and (b)  $\varphi = 90^\circ$  at 193.5 THz.

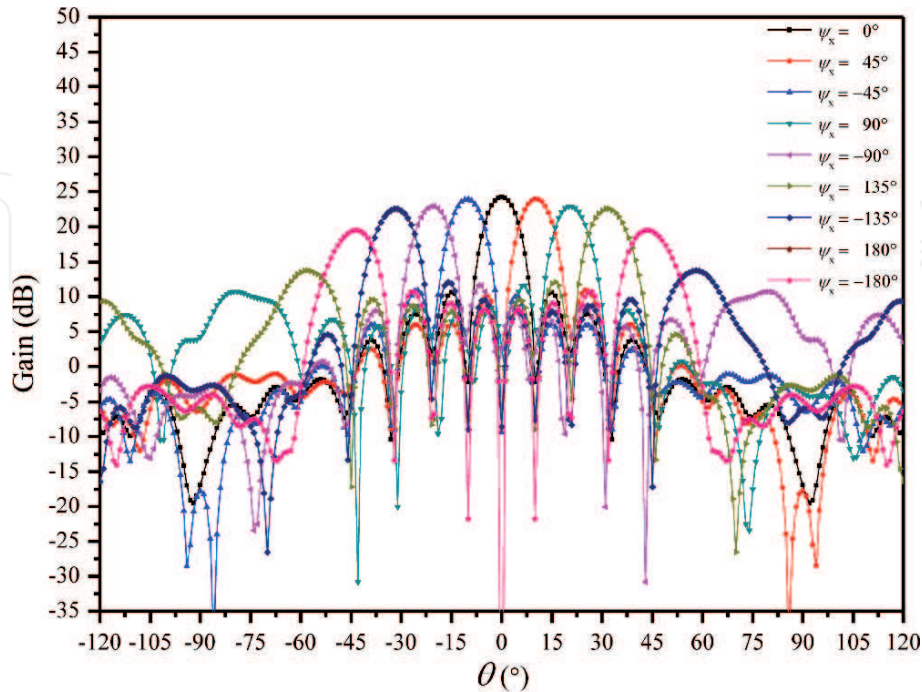


**Figure 21.**

Far-field beam steering in the  $\varphi = 0^\circ$  plane of the designed  $8 \times 8$  array with  $d_x = d_y = 0.7\lambda_0$  at 193.5 THz when  $\psi_x$  changes from  $-180^\circ$  to  $180^\circ$  and  $\psi_y$  is fixed at  $0^\circ$ .

changed, the beam steers in the  $\varphi = 90^\circ$  plane. As the phase difference  $\psi_y$  changes from  $-180.0^\circ$  to  $+180.0^\circ$ , the radiation direction of the light changes in a certain range of  $-45.0^\circ$  to  $+45.0^\circ$  at 193.5 THz.

Therefore, the designed  $8 \times 8$  array can be used to realize the beam steering with a steering range of  $\pm 44.0^\circ \times \pm 45.0^\circ$  by controlling the differences of  $\psi_x$  and  $\psi_y$ . Calculated by Eq. (1), an  $8 \times 8$  array with the element spacing of  $0.7\lambda_0$  along the  $x$ - and  $y$ -axis has a beam steering range of  $\pm 45.6^\circ \times \pm 45.6^\circ$ , which is basically consistent with the simulation results. At 193.5 THz, a far-field radiation pattern of the designed  $8 \times 8$  array is simulated when  $\psi_x = \psi_y = 45^\circ$ , as shown in **Figure 23**. It is clearly seen that an optical beam is radiated with an angle of  $\theta = 14.0^\circ$  and  $\varphi = 45^\circ$ .

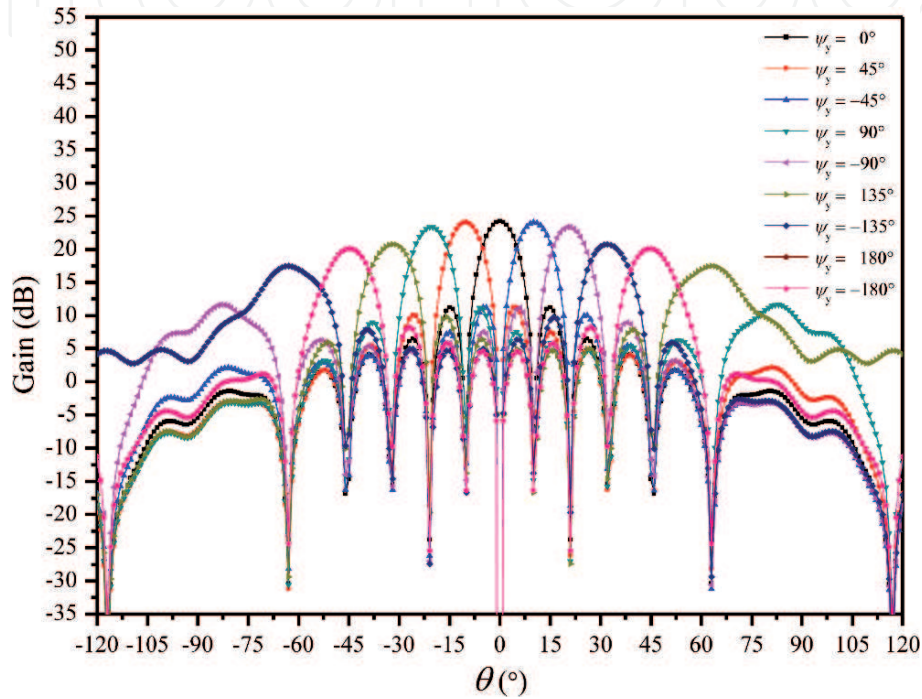


**Figure 22.** Far-field beam steering in the  $\varphi = 90^\circ$  plane of the  $8 \times 8$  array with  $d_x = d_y = 0.7\lambda_0$  at 193.5 THz when  $\psi_y$  changes from  $-180^\circ$  to  $180^\circ$  and  $\psi_x$  is fixed at  $0^\circ$ .

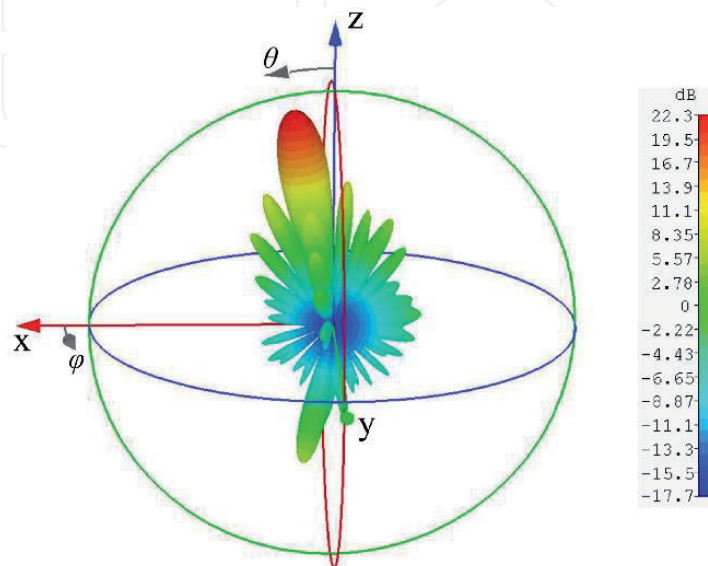


**Figure 23.** Far-field radiation pattern of the designed  $8 \times 8$  array with  $d_x = d_y = 0.7\lambda_0$  at 193.5 THz when  $\psi_x = \psi_y = 45^\circ$ .

## 4. Conclusion

In this chapter, we review the silicon-based optical nanoantennas and their applications in OPA for beam steering. In order to obtain an OPA with high gain and wide beam steering range, we propose a sub-wavelength plasmonic nanoantenna with an operating wavelength of 1550 nm. The proposed plasmonic nanoantenna consists of a silver block and a silicon block with a standard silicon waveguide for feeding light into the nanoantenna. On the basis of LSPR, the plasmonic nanoantenna radiates light vertically upward with a high gain of 8.45 dB at 1550 nm. There is a good impedance match between the plasmonic nanoantenna and the silicon waveguide in a frequency range from 176.7 to 248.5 THz. Furthermore, two nanoantenna arrays ( $1 \times 8$  and  $8 \times 8$ ) with the element spacing of  $0.7\lambda_0$  composed of the proposed plasmonic nanoantennas are designed, and their beam steering radiation patterns are studied in detail. The simulation results show that the  $1 \times 8$  array can be used to realize 1-D beam steering from  $-44.0^\circ$  to  $+44.0^\circ$  with a gain of 14.5 dB at 1550 nm, and the  $8 \times 8$  array can achieve a 2-D beam steering from  $-44.0^\circ$  to  $+44.0^\circ$  in one dimension and from  $-45.0^\circ$  to  $+45.0^\circ$  in the other dimension with a gain of 24.2 dB at 1550 nm.

The plasmonic nanoantenna we proposed is a good candidate for the extension of the nanoantenna array used in a large-scale OPA. Utilizing the proposed plasmonic nanoantenna, a 3-D array extend mode can be adopted to form an OPA with thousands of optical nanoantennas. We first make a 1-D OPA as a sub-layer, in which the optical power division network, phase shifters, and a 1-D plasmonic nanoantenna array are integrated in a plane. After that, such 1-D OPA layers are extended longitudinally. Therefore, a highly integrated OPA containing thousands of optical nanoantennas with sub-wavelength element spacing can be obtained theoretically to steer beam in a wide angle without grating lobes. However, the processing of the OPA with multilayer structure is limited by our micro/nanofabrication technology. We believe that with the development of micro/nanoprocessing technology, the large-scale OPA will be applied in various fields of optical communication, LiDAR, security monitoring, and display advertising, which will bring great benefits to human life.

## Acknowledgements

The authors would like to thank Dr. Zhihui Liu for her support in reviewing. This work is supported by Innovation Funds of China Aerospace Science and Technology (No. Y-Y-Y-GJGXXZ-18, No. Z-Y-Y-KJJGTX-17) and the 2017 Open Research Fund of Key Laboratory of Cognitive Radio and Information Processing, Ministry of Education, Guilin University of Electronic Technology (No. CRKL170202).

IntechOpen

### **Author details**

Tao Dong<sup>1,2\*</sup>, Yue Xu<sup>1,2</sup> and Jingwen He<sup>1,2</sup>

1 State Key Laboratory of Space-Ground Integrated Information Technology,  
Beijing, China

2 Beijing Institute of Satellite Information Engineering, Beijing, China

\*Address all correspondence to: [dongtaoandy@163.com](mailto:dongtaoandy@163.com)

### **IntechOpen**

© 2020 The Author(s). Licensee IntechOpen. This chapter is distributed under the terms of the Creative Commons Attribution License (<http://creativecommons.org/licenses/by/3.0>), which permits unrestricted use, distribution, and reproduction in any medium, provided the original work is properly cited. 

## References

- [1] Sun J, Timurdogan E, Yaacobi A, Hosseini ES, Watts MR. Large-scale nanophotonic phased array. *Nature*. 2013;**493**:195-199. DOI: 10.1038/nature11727
- [2] Abediasl H, Hashemi H. Monolithic optical phased-array transceiver in a standard SOI CMOS process. *Optics Express*. 2015;**23**:6509-6519. DOI: 10.1364/OE.23.006509
- [3] Sabouri S, Jamshidi K. Design considerations of silicon nitride optical phased array for visible light communications. *IEEE Journal of Selected Topics in Quantum Electronics*. 2018;**24**:1-7. DOI: 10.1109/JSTQE.2018.2836991
- [4] Poulton CV, Byrd MJ, Russo P, Timurdogan E, Khandaker M, Vermeulen D, et al. Long-range LiDAR and free-space data communication with high-performance optical phased arrays. *IEEE Journal of Selected Topics in Quantum Electronics*. 2019;**25**:1-8. DOI: 10.1109/JSTQE.2019.2908555
- [5] Raval M, Yaacobi A, Watts MR. Integrated visible light phased array system for autostereoscopic image projection. *Optics Letters*. 2018;**43**:3678-3681. DOI: 10.1364/OL.43.003678
- [6] McManamon PF, Dorschner TA, Corkum DL, Friedman LJ, Hobbs DS, Holz M, et al. Optical phased array technology. *Proceedings of the IEEE*. 1996;**84**:268-298. DOI: 10.1109/5.482231
- [7] Van Acoleyen K, Rogier H, Baets R. Two-dimensional optical phased array antenna on silicon-on-insulator. *Optics Express*. 2010;**18**:13655-13660. DOI: 10.1364/OE.18.013655
- [8] Kwong D, Hosseini A, Covey J, Zhang Y, Xu X, Subbaraman H, et al. On-chip silicon optical phased array for two-dimensional beam steering. *Optics Letters*. 2014;**39**:941-944. DOI: 10.1364/OL.39.000941
- [9] Christopher VP, Ami Y, Zhan S, Matthew JB, Michael RW. Optical phased array with small spot size, high steering range and grouped cascaded phase shifters. In: *Advanced Photonics Congress 2016 (IPR, NOMA, Sensors, Networks, SPPCom, SOF)*; 18-20 July 2016; Vancouver. Washington: OSA; 2016. IW1B.2
- [10] Doylend JK, Heck MJR, Bovington JT, Peters JD, Coldren LA, Bowers JE. Two-dimensional free-space beam steering with an optical phased array on silicon-on-insulator. *Optics Express*. 2011;**19**:21595-21604. DOI: 10.1364/OE.19.021595
- [11] Hutchison DN, Sun J, Doylend JK, Kumar R, Heck J, Kim W, et al. High-resolution aliasing-free optical beam steering. *Optica*. 2016;**3**:887-890. DOI: 10.1364/OPTICA.3.000887
- [12] Poulton CV, Byrd MJ, Raval M, Su Z, Li N, Timurdogan E, et al. Large-scale silicon nitride nanophotonic phased arrays at infrared and visible wavelengths. *Optics Letters*. 2017;**42**:21-24. DOI: 10.1364/OL.42.000021
- [13] Zhang Y, Ling Y, Zhang K, Gentry C, Sadighi D, Whaley G, et al. Sub-wavelength-pitch silicon-photonics optical phased array for large field-of-regard coherent optical beam steering. *Optics Express*. 2019;**27**:1929-1940. DOI: 10.1364/OE.27.001929
- [14] Guclu C, Boyraz O, Capolino F. Theory of optical leaky-wave antenna integrated in a ring resonator for radiation control. *Journal of Lightwave Technology*. 2017;**35**:10-18. DOI: 10.1109/JLT.2016.2626982

- [15] Zhao C, Zhang H, Zheng Z, Peng C, Hu W. Silicon optical-phased-array prototypes using electro-optical phase shifters. In: 2017 Conference on Lasers and Electro-Optics (CLEO); 14-19 May 2017; San Jose. Washington: OSA; 2017. SM10.4
- [16] Yoo B, Megens M, Sun T, Yang W, Chang-Hasnain CJ, Horsley DA, et al. A  $32 \times 32$  optical phased array using polysilicon sub-wavelength high-contrast-grating mirrors. *Optics Express*. 2014;22:19029-19039. DOI: 10.1364/OE.22.019029
- [17] Fatemi R, Abiri B, Khachaturian A, Hajimiri A. High sensitivity active flat optics optical phased array receiver with a two-dimensional aperture. *Optics Express*. 2018;26:29983-29999. DOI: 10.1364/OE.26.029983
- [18] Fatemi R, Khachaturian A, Hajimiri A. A nonuniform sparse 2-D large-FOV optical phased array with a low-power PWM drive. *IEEE Journal of Solid-State Circuits*. 2019;54:1200-1215. DOI: 10.1109/JSSC.2019.2896767
- [19] Iluz Z, Boag A. Wide-angle scanning optical linear phased array. In: 2015 IEEE International Conference on Microwaves, Communications, Antennas and Electronic Systems (COMCAS); 2-4 November 2015; Tel Aviv. New York: IEEE; 2015. pp. 1-2
- [20] Yousefi L, Foster AC. Waveguide-fed optical hybrid plasmonic patch nano-antenna. *Optics Express*. 2012;20:18326-18335. DOI: 10.1364/OE.20.018326
- [21] Kim M, Li Z, Yu N. Controlling light propagation in optical waveguides using one dimensional phased antenna arrays. In: 2014 Conference on Lasers and Electro-Optics (CLEO); 8-13 June 2014; San Jose. New York: IEEE; 2015. FW3C.4
- [22] Nia BA, Yousefi L, Shahabadi M. Integrated optical-phased array nanoantenna system using a plasmonic rotman lens. *Journal of Lightwave Technology*. 2016;34:2118-2126. DOI: 10.1109/JLT.2016.2520881
- [23] Xu Y, Dong T, He J, Wan Q. Large scalable and compact hybrid plasmonic nanoantenna array. *Optical Engineering*. 2018;57:087101. DOI: 10.1117/1.OE.57.8.087101
- [24] Johnson PB, Christy RW. Optical constants of the noble metals. *Physical Review B*. 1972;6:4370-4379. DOI: 10.1103/PhysRevB.6.4370
- [25] Eibert TF, Volakis JL. *Antenna Engineering Handbook*. 4th ed. New York: McGraw-Hill; 2007. pp. 10-968